Published March 2, 2017

The MICOS component Mic60 displays a conserved membrane-bending activity that is necessary for normal cristae morphology

Daryna Tarasenko,[1]* Mariam Barbot,[1]* Daniel C. Jans,[2,4] Benjamin Kroppen,[1] Boguslawa Sadowski,[5,6] Gudrun Heim,[3] Wiebke Möbius,[5,6] Stefan Jakobs,[2,4] and Michael Meinecke[1,7,8]

[1]Department of Cellular Biochemistry, University Medical Center Göttingen, 37073 Göttingen, Germany
[2]Department of Neurology, University Medical Center Göttingen, 37075 Göttingen, Germany
[3]Electron Microscopy Facility and [4]Department of NanoBiophotonics, Max Planck Institute for Biophysical Chemistry, 37077 Göttingen, Germany
[5]Department of Neurogenetics, Max Planck Institute of Experimental Medicine, 37075 Göttingen, Germany
[6]Cluster of Excellence Nanoscale Microscopy and Molecular Physiology of the Brain (CNMPB), 37073 Göttingen, Germany
[7]European Neuroscience Institute Göttingen, 37077 Göttingen, Germany
[8]Göttinger Zentrum für Molekulare Biowissenschaften, 37077 Göttingen, Germany

The inner membrane (IM) of mitochondria displays an intricate, highly folded architecture and can be divided into two domains: the inner boundary membrane adjacent to the outer membrane and invaginations toward the matrix, called cristae. Both domains are connected by narrow, tubular membrane segments called cristae junctions (CJs). The formation and maintenance of CJs is of vital importance for the organization of the mitochondrial IM and for mitochondrial and cellular physiology. The multisubunit mitochondrial contact site and cristae organizing system (MICOS) was found to be a major factor in CJ formation. In this study, we show that the MICOS core component Mic60 actively bends membranes and, when inserted into prokaryotic membranes, induces the formation of cristae-like plasma membrane invaginations. The intermembrane space domain of Mic60 has a lipid-binding capacity and induces membrane curvature even in the absence of the transmembrane helix. Mic60 homologues from α-proteobacteria display the same membrane deforming activity and are able to partially overcome the deletion of Mic60 in eukaryotic cells. Our results show that membrane bending by Mic60 is an ancient mechanism, important for cristae formation, and had already evolved before α-proteobacteria developed into mitochondria.

Introduction

Mitochondria are ubiquitous organelles with a central role not only in many metabolic pathways, but also in the regulation and maintenance of cellular health. The outer membrane (OM) functions as a molecular sieve and as a mechanical barrier against the rest of the cell. The mitochondrial inner membrane (IM) is an energy-coupling membrane and the main location for cellular ATP production. To harbor large quantities of the F_1F_O-ATP synthase as well as oxidative phosphorylation complexes, the IM possesses a larger surface area than the OM, which results in a complex folded IM architecture. The IM can be subdivided into two regions: the inner boundary membrane, which runs in close proximity to the OM, and the cristae membranes, which are invaginations toward the mitochondrial matrix. Narrow, highly curved tubular membrane segments called cristae junctions (CJs) physically connect the inner boundary and cristae membranes. CJs are presumably important for sequestering the IM into distinct functional domains by imposing a diffusion barrier and thereby contributing to an uneven protein distribution (Mannella, 2006; Vogel et al., 2006; Wurm and Jakobs, 2006; Strauss et al., 2008; Rabl et al., 2009). Additionally, CJs play a key role in the regulation of the intrinsic apoptotic pathway (Scorrano et al., 2002; Pellegrini and Scorrano, 2007). Little is known about the formation of CJs, and a molecular understanding of how membrane deformation occurs at CJs is just emerging. The recently identified multisubunit mitochondrial contact site and cristae organizing system (MICOS) complex resides at CJs (Rabl et al., 2009; Harner et al., 2011; Hoppins et al., 2011; Jans et al., 2013; Guarani et al., 2015) and plays a crucial role in forming and maintaining the architecture of the

*D. Tarasenko and M. Barbot contributed equally to this paper.

Correspondence to Michael Meinecke: michael.meinecke@med.uni-goettingen.de

Abbreviations used: CJ, cristae junction; DDM, *n*-dodecyl β-D-maltoside; ENTH, epsin N-terminal homology; GUV, giant unilamellar vesicle; IM, inner membrane; IMS, intermembrane space; LUV, large unilamellar vesicle; MBP, maltose-binding protein; MICOS, multisubunit mitochondrial contact site and cristae organizing system; OM, outer membrane; PK, proteinase K; RD, relative distribution.

© 2017 Tarasenko et al. This article is distributed under the terms of an Attribution–Noncommercial–Share Alike–No Mirror Sites license for the first six months after the publication date (see http://www.rupress.org/terms/). After six months it is available under a Creative Commons License (Attribution–Noncommercial–Share Alike 4.0 International license, as described at https://creativecommons.org/licenses/by-nc-sa/4.0/).

The Rockefeller University Press $30.00
J. Cell Biol.
https://doi.org/10.1083/jcb.201609046

THE JOURNAL OF CELL BIOLOGY

Downloaded from on March 7, 2017

Published March 2, 2017

IM (Harner et al., 2011; Hoppins et al., 2011; von der Malsburg et al., 2011; Alkhaja et al., 2012). The two MICOS core components, Mic10 and Mic60, are both well conserved in eukaryotes (Muñoz-Gómez et al., 2015; Huynen et al., 2016). Mic10 forms high–molecular weight oligomers and was shown to induce high degrees of membrane curvature in model membranes as well as to influence IM architecture in vivo (Barbot et al., 2015; Bohnert et al., 2015; Barbot and Meinecke, 2016). The second core component, Mic60, interacts with various proteins in the IM and the OM (Xie et al., 2007; Harner et al., 2011; Hoppins et al., 2011; von der Malsburg et al., 2011; Bohnert et al., 2012; Körner et al., 2012; Ott et al., 2012; Zerbes et al., 2012). The current model for the MICOS core components is that Mic60 is important for positioning the MICOS at CJs and for connecting IMs and OMs, whereas Mic10 is mainly responsible for shaping the IM at CJs. Nonetheless, Mic60 is the evolutionarily oldest MICOS component and the only one with homologues in α-proteobacteria, the ancestors of mitochondria, that often display intracytoplasmic membrane structures (Bock and Heinrich, 1971; Tucker et al., 2010; Nudelman and Zarivach, 2014; Muñoz-Gómez et al., 2015; Huynen et al., 2016). The absence of Mic60 causes a loss of CJs (John et al., 2005; Harner et al., 2011; Hoppins et al., 2011; von der Malsburg et al., 2011), and Mic60 overexpression leads to highly branched cristae membranes (Rabl et al., 2009; Bohnert et al., 2015). Hence, we asked whether, in addition to its role as an interaction hub, Mic60 directly influences IM morphology.

Results and discussion

To investigate a possible role for Mic60 in membrane deformation and CJ formation, we cloned and expressed full-length *Saccharomyces cerevisiae* Mic60 (Mic60$^{S.c.}$; Fig. 1 A) without its mitochondrial targeting sequence in *Escherichia coli* and purified it to homogeneity (Fig. 1 B). As full-length Mic60 contains a transmembrane domain, it was sorted into inclusion bodies. After purification, the protein was solubilized in *n*-dodecyl β-D-maltoside (DDM), a mild detergent known to preserve the tertiary structures of integral membrane proteins (Privé, 2007), and circular dichroism spectroscopy analysis revealed a mainly α-helical structure of Mic60 in DDM (Fig. 1 C). Mic60 was integrated into large unilamellar vesicles (LUVs) by a detergent-mediated reconstitution protocol (Krüger et al., 2012; Montilla-Martinez et al., 2015). Reconstitution success was analyzed by flotation of the vesicles in a noncontinuous Histodenz density gradient and subsequent carbonate extraction (Fig. 1, D–F). Conversely to empty LUVs, Mic60-containing vesicles enriched at different boundary layers of the gradient. This effect was observed before for membrane curvature inducing bin-amphiphysin-Rvs (BAR) domains and for the transmembrane protein Mic10 (Barbot et al., 2015). Similar flotation patterns could be observed when LUVs were incubated with the epsin N-terminal homology (ENTH) domain of the peripheral membrane protein epsin1 (Fig. 1, G–I), another molecule that is known to induce high degrees of membrane curvature in model membranes (Fig. S1 E; Gleisner et al., 2016). As a negative control, another mitochondrial IM protein with a similar topology to Mic60, but not involved in membrane remodeling processes, namely Tim50, was integrated into LUVs, and proteoliposomes floated similarly to empty vesicles (Fig. 1, G–I).

We next asked whether the complex flotation pattern is an indication of the changed morphologies of Mic60-containing LUVs. When analyzed by EM, Mic60 proteoliposomes showed broad structural changes. Compared with the round control vesicles, we frequently observed long, branched, tubular membrane structures with diameters between 10 and 20 nm (Figs. 2 A and S1 G), similar dimensions as has been observed for the inner diameter of CJs (Mannella, 2006). These structures are specific to membrane-inserted Mic60, as LUVs that had undergone mock reconstitution or Tim50-containing vesicles remained unchanged in their overall round appearance (Fig. 2 A). To further underline that membrane deformation is specific and not a result of molecular crowding by a large protein domain at the membrane surface, Mic60 and Tim50 were reconstituted with the same molar protein/lipid ratio of 1:450, and no signs of membrane deformation were observed when Mic60 was reconstituted in a molar protein/lipid ratio below 1:900 (Fig. S1, G and H). A two-step flotation gradient (Fig. S1 A) with subsequent carbonate resistance experiments (Fig. S1 B) showed that both proteins coflotate with liposomes in comparable amounts and that both proteins are efficiently membrane integrated. Proteinase K (PK) digestion experiments showed that Mic60 and Tim50 are both inserted unidirectionally into liposomes, with Mic60 exposing its intermembrane space (IMS) domain to the outside of the vesicle, whereas Tim50 exposes its soluble domain to the inside of liposomes (Fig. S1, C and D). The Mic60-dependent changes in membrane structure can also be observed in bulk, as dynamic light scattering experiments revealed broad changes in LUV size distribution in the presence of Mic60 (Fig. 2 B). Similar results were obtained with LUVs in the presence of the ENTH domain (Fig. S1 F). To specifically correlate membrane deformation with the presence of Mic60, we generated giant unilamellar vesicles (GUVs) with incorporated fluorescently labeled Mic60. Mic60-containing GUVs showed changed morphologies when compared with vesicles generated with the same protocol but in the absence of protein or with integrated fluorescently labeled Tim50. The presence of Mic60 mainly led to the appearance of internal vesicular membrane structures of different sizes (Fig. 2, C and D). In several cases, onion-like phenotypes were observed with connections between the different membrane layers (Figs. 2 D and S1 I). Altogether, these data show that Mic60 is able to affect the morphology of various model membranes.

If Mic60-dependent membrane deformation is relevant for mitochondrial cristae formation, the protein should be able to deform membranes in vivo and to induce cristae-like membrane structures de novo. To test this hypothesis, we expressed full-length Mic60 in *E. coli* as a maltose-binding protein (MBP) fusion construct (Fig. S2 E, top). This MBP construct contains a targeting sequence and is exported to the periplasm. The hydrophobic membrane segment of Mic60 serves as a stop-transfer signal and is trapped and released in the plasma membrane (Hu et al., 2011; Walser et al., 2012). As such, Mic60 is targeted to the plasma membrane. We subsequently analyzed the morphology of *E. coli* cells by EM. Although control *E. coli* cells did not show internal membrane structures (Fig. 3 A), MBP-Mic60–expressing cells displayed clear invaginations from the plasma membrane toward the cytoplasm (Fig. 3 B), leading to intracytoplasmic membrane structures. Interestingly, beside tubular membrane invaginations, we frequently observed vesicular membrane structures, emulating the effect that Mic60 has on GUVs. Cell fractionation experiments showed that Mic60

Downloaded from on March 7, 2017

Published March 2, 2017

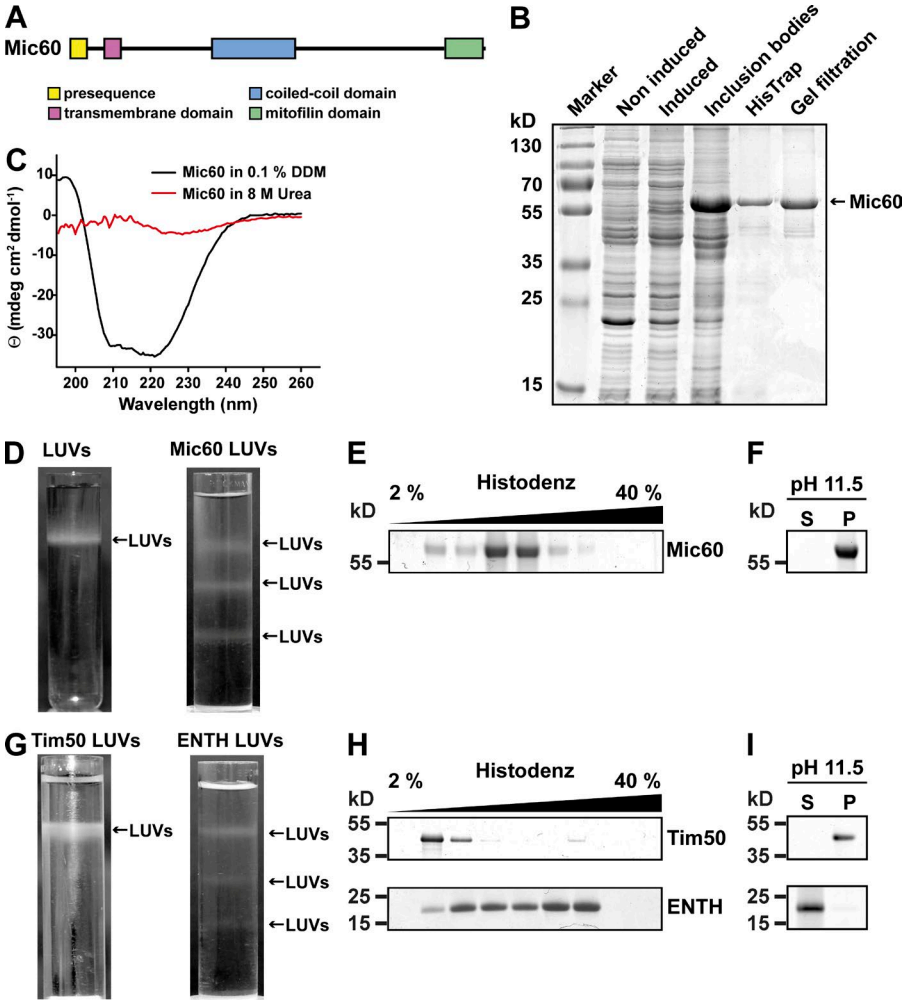

Figure 1. **Purification and reconstitution of *S. cerevisiae* Mic60.** (A) Domain architecture of Mic60 *S. cerevisiae*. (B) Expression and purification of recombinant Mic60 analyzed by SDS-PAGE with subsequent Coomassie Brilliant Blue staining. (C) Circular dichroism spectra of Mic60 in urea and renatured in DDM. mdeg, milidegree of molar elliptisity. (D) Flotation assay of empty LUVs and Mic60-containing vesicles as indicated, separated in a noncontinuous Histodenz density gradient. (E) Fractionation of the Histodenz density gradient centrifugation of Mic60-containing vesicles analyzed by SDS-PAGE Coomassie Brilliant Blue staining. (F) Sodium carbonate extraction assay of Mic60-containing LUVs analyzed by SDS-PAGE Coomassie Brilliant Blue staining. (G) Flotation assay of LUVs containing Tim50 and the epsin1 ENTH domain as indicated, separated in a noncontinuous Histodenz gradient. (H) Fractionation of floated samples from G analyzed by SDS-PAGE Coomassie Brilliant Blue staining. (I) Sodium carbonate extraction assay of Tim50- and ENTH-containing LUVs analyzed by SDS-PAGE Coomassie Brilliant Blue staining. P, pellet; S, supernatant.

is indeed efficiently integrated into the plasma membrane (Fig. 3 D). To correlate the internal membrane structures with the presence of Mic60, we performed immunogold labeling with subsequent EM analysis, showing a clear colocalization of Mic60 and plasma membrane invaginations (Fig. 3, C and E; and Fig. S2 A). Neither the overexpression of MBP alone nor the presence of plasma membrane–targeted Tim50, Tom20, or the multispanning transmembrane protein Tim23 led to invaginated plasma membranes or internal vesicular or tubular membrane structures in *E. coli* cells (Figs. 3 F and S2, B–D). To analyze whether the transmembrane domain of Mic60 is necessary for membrane deformation, we expressed the IMS domain of Mic60 ($Mic60^{IMS}$) as an MBP fusion protein, thereby targeting $Mic60^{IMS}$ to the periplasmic space of *E. coli* (Fig. S2 E, bottom). EM and immunogold labeling analysis revealed $Mic60^{IMS}$-dependent intracytoplasmic membrane structures, reminiscent of cristae membranes, diverging from the plasma membrane toward the cytoplasm (Fig. 3 G). As the transmembrane domain of Mic60 is dispensable for plasma membrane invagination, we asked whether $Mic60^{IMS}$ directly interacts with membranes to change their morphology. We tested whether $Mic60^{IMS}$ has a lipid-binding capacity and therefore incubated LUVs with $Mic60^{IMS}$ and subsequently performed flotation assays. Not only did $Mic60^{IMS}$ bind to liposomes (Fig. S2 F), but when these LUVs were investigated by EM, long tubular membrane structures with diameters between 10 and 20 nm could be observed (Fig. 3 H). Hence, Mic60 is able to form membrane invaginations in vivo, and the membrane remodeling activity is, at least partially, located in the IMS domain of Mic60.

It was recently found that Mic60 is the evolutionarily oldest subunit of the MICOS complex and that prokaryotic Mic60 homologues are present in α-proteobacteria, the endosymbiotic ancestors of mitochondria (Muñoz-Gómez et al., 2015; Huynen et al., 2016). The coiled-coil domain and the mitofilin domain are both found in eukaryotes and α-proteobacteria (Muñoz-Gómez et al., 2015), and hence the IMS segment of $Mic60^{S.c.}$ is especially structurally conserved (Fig. S3 A; Muñoz-Gómez et al., 2015). As several α-proteobacteria show intracytoplasmaic membrane structures (Komeili et al., 2004; Tucker et al., 2010) that look similar to the plasma membrane structures induced by Mic60 in *E. coli* cells, we asked whether a membrane-deforming activity can already be found in α-proteobacterial Mic60 homologues. We therefore cloned the Mic60 homologues of *Paracoccus denitrificans* ($Mic60^{P.d.}$) and *Rhodobacter sphaeroides* ($Mic60^{R.s.}$) as MBP fusion proteins and expressed them in *E. coli*. Both proteins were targeted to the plasma membrane (Fig. 4, B and D), and EM analysis of these cells revealed intracytoplasmic membranes invaginating from the plasma membrane, leading to membrane-bound and free vesicular and tubular structures (Fig. 4, A and C). Interestingly, similar structures can be found in *R. sphaeroides*, where plasma membrane–bound and free membrane vesicles were observed (Tucker et al., 2010). A further link between Mic60 and such plasma membrane invaginations is provided by the finding that $Mic60^{R.s.}$ was

Downloaded from on March 7, 2017

Published March 2, 2017

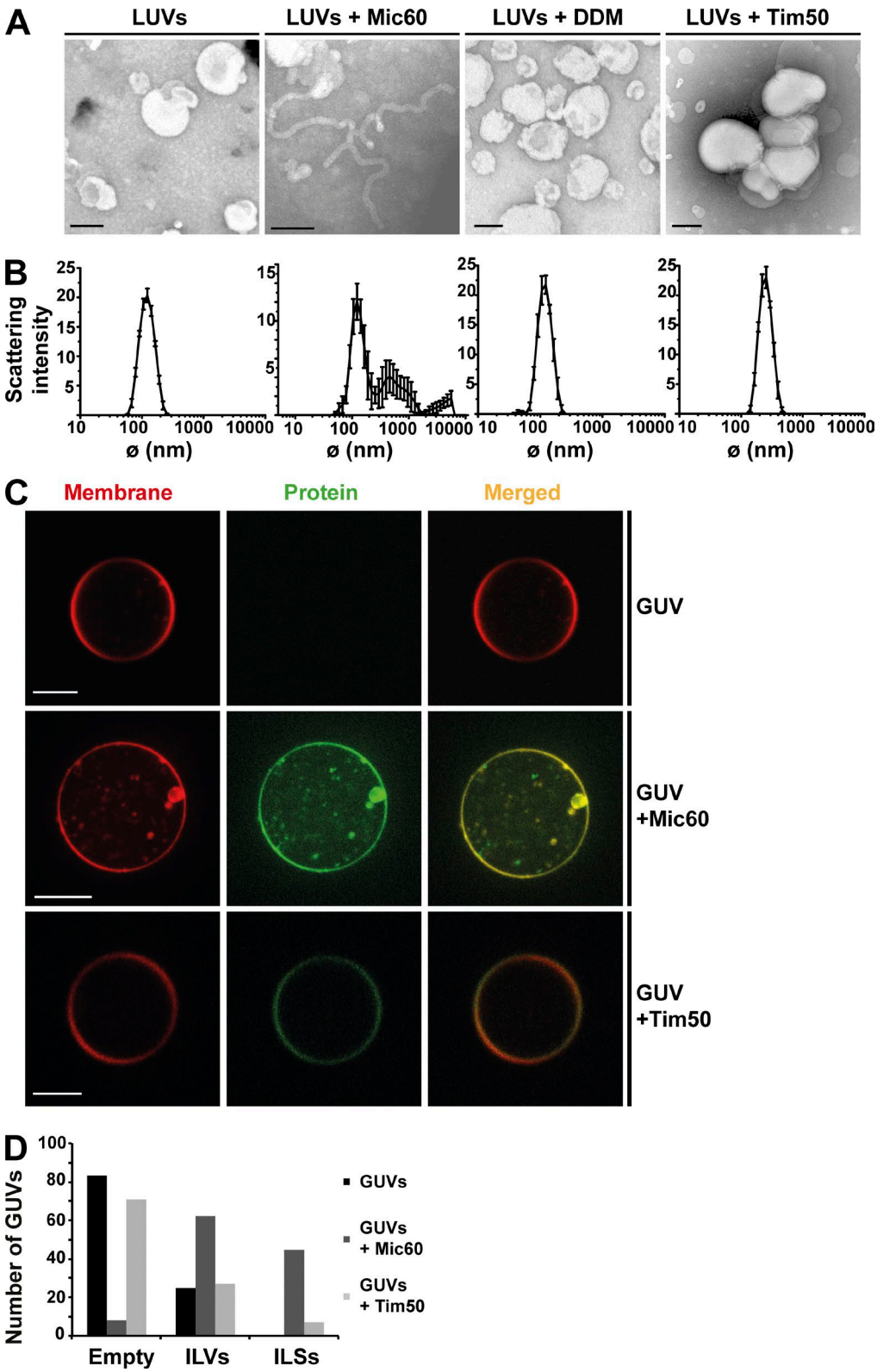

Figure 2. **Mic60 induces high degrees of curvature in model membranes.** (A) Electron micrographs of negatively stained LUVs with the indicated additives. (B) Dynamic light scattering analysis of LUV size distribution. Error bars represent SEM. (C) GUVs in the absence and presence of the indicated proteins. GUVs were labeled with rhodamine-PE, and proteins were labeled with Alexa Fluor 488. (A and C) Bars: (A) 100 nm; (C) 10 µm. (D) Histogram of GUV morphologies in the absence and presence of various proteins. For each condition, a minimum of 100 GUVs from three preparations were counted, and the values given in the histogram are absolute numbers. ILVs, intraluminal vesicles; ILSs, intraluminal sheets.

Downloaded from on March 7, 2017

Published March 2, 2017

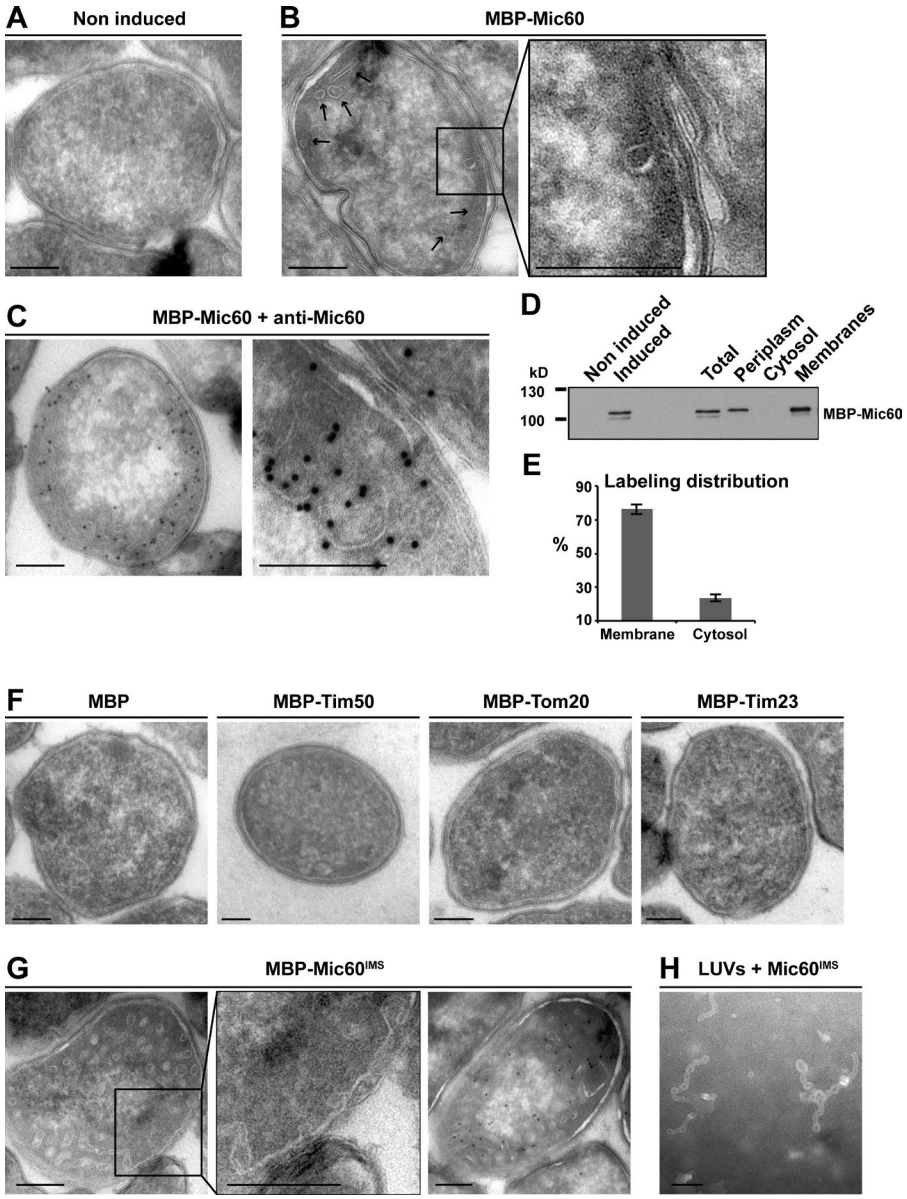

Figure 3. **Mic60 induces membrane invaginations in prokaryotic membranes.** (A) Electron micrograph of an *E. coli* cell. (B) Electron micrograph of an *E. coli* cell expressing MBP-Mic60. Arrows mark Mic60-induced intracytoplasmaic membranes. The zoomed image shows that membranes invaginate from the plasma membrane. (C) Electron micrographs of immunogold-labeled *E. coli* cells (anti-Mic60). (D) Cell fractionation of *E. coli* cells expressing MBP-Mic60 analyzed by Western blot. Anti-MBP antibody was used. (E) Quantification of the immunogold labeling. The histogram represents RD. RD was evaluated by counting the number of specific gold particles (1,481) in 27 *E. coli* cells (n = 27). Error bars represent SD. (F) Electron micrographs of *E. coli* cells expressing the indicated proteins. (G) Electron micrographs of *E. coli* cells expressing the IMS domain of Mic60 as an MBP fusion protein. The zoomed image shows internal membrane structures connected to the plasma membrane. The right image shows an immunogold-labeled *E. coli* cell. (H) EM image of LUVs in the presence of $Mic60^{IMS}$. Bars, 100 nm.

found to be localized, among others, in the membranes of these vesicles (D'Amici et al., 2010). To directly show that α-proteobacterial Mic60 is able to induce membrane curvature, we purified the recombinant proteins from *E. coli* and integrated them into LUVs using a detergent-mediated reconstitution protocol (Fig. 4 F). Vesicles containing either $Mic60^{P.d.}$ or $Mic60^{R.s.}$ displayed broad morphological changes, where round liposomes were converted into elongated, tubular membrane structures (Fig. 4 E). To further investigate whether the ability to shape cristae membranes by forming CJ-like structures is evolutionarily conserved, we expressed $Mic60^{P.d.}$ and $Mic60^{R.s.}$ in *S. cerevisiae* strains lacking wild-type Mic60 and targeted them to mitochondria (Fig. S3 B). Expression of $Mic60^{P.d.}$ and $Mic60^{R.s.}$, if at all, only led to a very mild restored growth of yeast cells on a nonfermentable carbon source (Fig. S3 C). Hence, we next asked whether the ultrastructural *mic60Δ* phenotype could be rescued by expressing $Mic60^{P.d.}$ or $Mic60^{R.s.}$. *mic60Δ* cells showed at least 50% mitochondria with altered morphologies, characterized by stacked or onion-shaped cristae membranes (Fig. 4 G, bottom). The expression of α-proteobacterial Mic60s led to a partial rescue of this phenotype (Fig. 4, G and H) similar though not as strong as $Mic60^{S.c.}$ expressed from a plasmid in *mic60Δ* cells (Fig. 4, G and H). Similar findings were obtained when analyzing the overall mitochondrial network morphology of the various yeast strains using live-cell microscopy. Wild-type cells show tubular mitochondria that are occasionally interconnected, whereas the deletion of *mic60* leads to a fragmented network. Expression of $Mic60^{S.c.}$ rescues the *mic60Δ* phenotype, as does expression of $Mic60^{P.d.}$ and $Mic60^{R.s.}$, though the rescue of the overall network morphology mediated by the expression of the α-proteobacterial proteins appears to be less pronounced on average (Fig. 4 G, top). The significant rescue of the mitochondrial ultrastructure with, at best, a slight effect on the growth phenotype may be explained by the known dual function of Mic60. Although Mic60 is clearly required for keeping cristae membranes connected to the inner boundary membrane, it also interacts with several proteins in the OM and IMS. We postulate that the membrane-shaping activity of Mic60 is important for normal cristae membrane structure and is well conserved even in α-proteobacteria, whereas the ability

Downloaded from on March 7, 2017

Published March 2, 2017

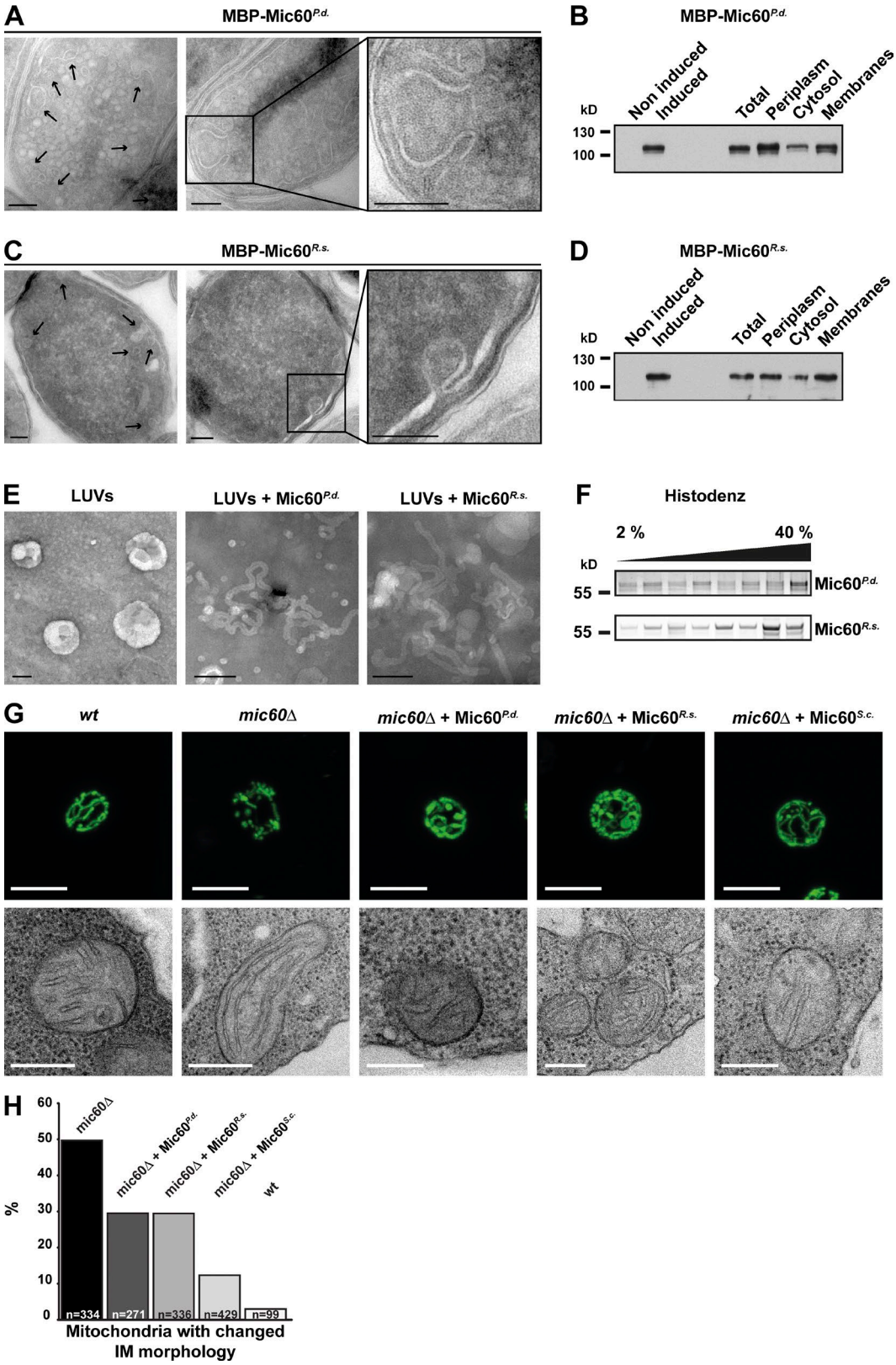

Figure 4. **α-Proteobacterial Mic60 homologues deform the membrane in vitro and in vivo and rescue depletion of Mic60 in eukaryotic cells.** (A) Electron micrographs of *E. coli* cells expressing Mic60 from *P. denitrificans* as an MBP fusion protein. (B) Cell fractionation of *E. coli* cells expressing Mic60$^{P.d.}$ analyzed by Western blot. Anti-MBP antibody was used. (C) Electron micrographs of *E. coli* cells expressing Mic60 from *R. sphaeroides* as an MBP fusion protein. (A and C) Arrows mark intracytoplasmaic membranes. Zoomed images show internal membrane structures connected to the plasma membrane. (D) Cell fractionation of *E. coli* cells expressing Mic60$^{R.s.}$ analyzed by Western blot. Anti-MBP antibody was used. (E) Electron micrographs of negatively stained LUVs in the absence or presence of the indicated proteins. (F) Fractionation of floated Mic60$^{P.d.}$- and Mic60$^{R.s.}$-containing LUVs analyzed by SDS-PAGE Coomassie Brilliant Blue staining. (G) Representative fluorescent microscopy images (top) and EM images (bottom) of yeast cells with the indicated

Downloaded from on March 7, 2017

Published March 2, 2017

to form protein–protein interactions in mitochondria probably evolved at a later time point. Altogether, our results show that Mic60 shapes mitochondrial IMs and that Mic60-dependent cristae formation evolved before endosymbiosis more than 1.5 billion years ago. The findings also suggest that mitochondrial cristae are homologous to α-proteobacterial intracytoplasmic membranes and that Mic60 plays a major role in the formation of both structures.

We recently found that the second MICOS core component, Mic10, is able to induce membrane curvature, which is important for CJ formation (Barbot et al., 2015). Therefore, the result that Mic60 is able to deform membranes and induce cristae-like membrane structures is surprising. Clearly, both proteins are using different molecular mechanisms to bend membranes. Mic10 probably spans the IM in a wedge-like topology (Barbot et al., 2015; Barbot and Meinecke, 2016), thereby occupying a larger surface on one side of the membrane than on the other. For Mic60-dependent curvature induction, the transmembrane domain seems to be dispensable, and it is tempting to speculate that it uses similar membrane-bending mechanisms as described for other peripheral membrane proteins (Zimmerberg and Kozlov, 2006). The fact that Mic60 is already present in α-proteobacteria that display intracytoplasmic membrane structures suggests a hierarchy where Mic60-dependent membrane deformation was developed before Mic10. As the formation and maintenance of eukaryotic CJs are of vital importance for mitochondrial and cellular physiology, they have to be tightly regulated. It is therefore conceivable that more than one membrane-shaping molecule is involved in this process to ensure a regulatory fine tuning. This is in line with the observation that in other membrane remodeling processes, such as clathrin-mediated endocytosis, or in the formation of the endoplasmic reticulum, various molecules with the ability to deform membranes are found (McMahon and Boucrot, 2011; Shemesh et al., 2014; Simunovic and Bassereau, 2014). Adding a further level of complexity, it is becoming clear that both MICOS and mitochondrial lipids are important for a correctly shaped IM (Friedman et al., 2015; Aaltonen et al., 2016). Our results explain the mitochondrial phenotypes that accompany changed Mic60 expression levels. Deletion of Mic60 leads to a reduction of highly curved CJs (Harner et al., 2011; Hoppins et al., 2011; von der Malsburg et al., 2011). Mic60 overexpression results not only in an increased number of CJs, but also in highly branched cristae membranes (Rabl et al., 2009; Bohnert et al., 2015), suggesting that the role of Mic60 in CJ formation is balanced by other proteins, likely Mic10. The MICOS complex was recently found to be made up of different modules, where a Mic10–Mic12–Mic26–Mic27 subcomplex is connected to a Mic60–Mic19 subcomplex, probably by Mic12 and/or Mic19 (Friedman et al., 2015; Guarani et al., 2015; Zerbes et al., 2016). Deletion of Mic12 destabilizes the connection between the two subcomplexes (Guarani et al., 2015; Zerbes et al., 2016) and has a similar, though milder, phenotype as the depletion of either Mic60 or Mic10 (Harner et al., 2011; Hoppins et al., 2011; von der Malsburg et al., 2011). We therefore hypothesize that an interplay between the two membrane-deforming proteins Mic60 and Mic10 is necessary for normal cristae formation, which is underlined by the fact that Mic60 and Mic10 are the most conserved proteins of the MICOS complex and can be found in every major lineage of eukaryotes (Muñoz-Gómez et al., 2015; Huynen et al., 2016).

Materials and methods

Recombinant protein expression and purification

Coding sequences of full-length Tim50, Mic60, and Mic60^{IMS} from *S. cerevisiae* were cloned into pPROEX HTc vector as fusion with N-terminal 6×His-tag and were expressed in BL21(DE3) *E. coli* in the presence of 1 mM IPTG for 3 h at 37°C. Cells were harvested and insoluble inclusion bodies were isolated. Purified inclusion bodies were dissolved in 8 M urea, 40 mM imidazole, 100 mM NaCl, 10 mM Tris-HCl, and 2 mM DTT buffer, pH 8, and subsequently applied onto a NiNTA-agarose column (GE Healthcare). Bound protein was eluted with 8 M urea, 500 mM imidazole, 100 mM NaCl, 10 mM Tris-HCl, and 2 mM DTT buffer, pH 8. Protein-containing fractions were collected and additionally subjected to size-exclusion chromatography using a HiLoad 16/600 Superdex 200 pg column (GE Healthcare). Purified proteins were refolded by dialyzing against 0.1% DDM, 150 mM NaCl, and 20 mM Hepes buffer, pH 7.4.

The coding sequence of the ENTH domain (epsin1, aa 1–164) from *Rattus norvegicus* was cloned into pGEX-6P-2 vector as an N-terminal GST-fusion protein and expressed in BL21(DE3) *E. coli* in the presence of 1 mM IPTG for 3 h at 30°C. The cells were harvested, resuspended in 150 mM NaCl and 50 mM Hepes buffer, pH 7.4, supplemented with EDTA-free protease inhibitor cocktail (Roche), and subsequently ruptured by three passes through the EmulsiFlex high-pressure homogenizer (Avestin) at 15,000–17,000 psi and 103–117 MPa. Total cell lysate was cleared by ultracentrifugation at 150,000 *g* and 4°C for 1 h. Supernatant was applied onto a glutathione Sepharose column (GE Healthcare). Bound protein was eluted with 100 mM NaCl and Tris-HCl buffer, pH 8, supplemented with 10 mM reduced glutathione. GST-tag was removed by PreScission protease cleavage for 10 h at 4°C. The ENTH domain and free GST were separated on an anion exchanger Q Sepharose Fast Flow chromatography column (GE Healthcare) by gradient elution with high-salt buffer (1 M NaCl and 20 mM Hepes, pH 8) and low-salt buffer (50 mM NaCl and 20 mM Hepes, pH 8). ENTH domain–containing fractions were applied onto a size-exclusion chromatography HiLoad 16/600 Superdex 75 pg column (GE Healthcare), using 200 mM NaCl and 10 mM Hepes, pH 7.4, as a running buffer.

Proteoliposomes preparation

L-α-Phosphatidylcholine (PC), L-α-phosphatidylethanolamine (PE), L-α-phosphatidylinositol (PI), L-α-phosphatidylserine (PS), cardiolipin (CL), and 1,2-dioleoyi-s-glycero-3-phosphoethanolamine (DOPE) were purchased from Avanti Polar Lipids, Inc. 20% DOPE/80% PC, 20% DOPE/65% PC/15% CL, 60% PC/20% PE/15% PI/5% PS, and 45% PC/20% PE/15% PI/5% PS/15% CL lipid mixtures were dried

genetic backgrounds and mitochondrial ultrastructures. (A, C, E, and G) Bars: (A, C, and E) 100 nm; (G, top) 2.5 µm; (G, bottom) 300 nm. (H) Quantitative evaluation of the mitochondrial IM ultrastructure as detected in cell sections. Mitochondria with at least one clear connection to the inner boundary membrane (see *wild-type* [*wt*] EM image) were counted as unchanged. Those with stacked or onion-shaped cristae membranes (see *mic60Δ* EM image) and without connections to the boundary membrane were counted as changed. The given values are absolute numbers provided by the counting of mitochondria (number of mitochondria as indicated in the figure) with different structural features.

Downloaded from on March 7, 2017

Published March 2, 2017

under continuous N_2 flow to form thin lipid films and additionally dried in a desiccator for at least 3 h. Lipid films were hydrated in 150 mM NaCl and 20 mM Hepes buffer, pH 7.4. LUVs were formed by repeated freeze–thaw cycles, followed by extrusion through a 100-nm diameter polycarbonate filter (Whatman). Protein was added to presolubilized liposomesin 0.1% DDM LUVs with a molar protein/lipid ratio of 1:450 in 350 µl incorporation mixture. Proteoliposomes were formed by DDM depletion by using detergent-adsorbent Bio-Beads SM-2 Resin (Bio-Rad Laboratories).

Flotation assay and sodium carbonate extraction

Flotation assay was performed in nonionic Histodenz density gradient (Sigma-Aldrich). Proteoliposomes were placed on the bottom of the ultracentrifugation tubes, and the noncontinuous 40/20/10/5/2% Histodenz density gradient was built up from high density toward low. Proteoliposomes were subjected to centrifugation for 1 h at 150,000 *g* and 4°C. Afterward, gradient was dissected into separate fractions, precipitated with 10% TCA, and analyzed by SDS-PAGE. For sodium carbonate extraction, liposomes containing interfaces of the Histodenz layers were collected, incubated with ice-cold 20 mM Na_2CO_3 for 30 min on ice, and centrifuged for 30 min at 150,000 *g* and 4°C. Total amounts of pellets and TCA-precipitated supernatants were analyzed by SDS-PAGE.

Dynamic light scattering

Liposomes were analyzed on a Zetasizer Nano S system (Malvern Instruments). Single measurements consisted of 20 repetitions over 10 min. Error was calculated as the standard error of averaged values from at least three independent measurements.

EM of liposomes

Liposomes were placed on carbon-coated grids (Agar Scientific) and contrasted with 5% uranyl acetate solution. Electron microphotographs were obtained with a transmission electron microscope (JEM 1011; JEOL). Images were taken with an Orius SC1000 A charge-coupled device camera using image processing software (Gatan).

Orientation of Mic60 and Tim50 in proteoliposomes

Membrane-reconstituted N-terminally 6×His-tagged Mic60 and Tim50 topology was assessed by PK accessibility to exposed domains according to van der Laan et al. (2007) with modifications. Proteoliposomes were floated in two-step (40% and 2%) Histodenz density gradient by centrifugation for 1 h at 150,000 *g* and 4°C. Mic60 and Tim50 proteoliposomes were collected from the interface of the Histodenz layers. The samples were diluted in 8 vol of liposome hydration buffer and were collected by centrifugation for 30 min at 170,000 *g* and 4°C. The pellets were resuspended in liposome hydration buffer and were split into separate tubes for PK digestion and control. For PK experiments, proteoliposomes were digested with 40 µg/ml PK for 20 min on ice. PK activity was subsequently blocked by 2 mM PMSF for 10 min on ice. Proteoliposomes were collected by centrifugation for 30 min at 170,000 *g* and were washed with liposome hydration buffer. The supernatants were TCA precipitated. Both washed and TCA-precipitated pellets were resuspended in SDS sample loading buffer containing 1 mM PMSF and boiled for 5 min at 95°C. For control Mic60 and Tim50 PK digestion, the same amounts of protein as for the proteoliposomes were used. After PK digestion and PK activity blocking as described above, the protein samples were resuspended in SDS sample loading buffer containing 1 mM PMSF and boiled for 5 min at 95°C. After SDS-PAGE, the gel was blotted and immunodecorated with primary mouse monoclonal antibody against His-tag (Sigma-Aldrich).

GUV preparation and imaging

GUVs were produced using the electroformation technique. Proteoliposomes were resuspended in 5 mM NaCl and 10 mM Hepes buffer, pH 7.4, to a final 0.5-mg/ml concentration of lipids, and small droplets were spotted on indium tin oxide (ITO)–coated glass slides. Proteoliposomes were partially dehydrated for 2 h in a desiccator under the saturated vapor pressure of KCl solution. The GUV generation chamber was assembled by separating two ITO-coated slides by 0.6 ml of a 300-mM glucose solution and thin rubber spacer. For electroformation, an alternating current electric field was generated by a pulse generator connected to the slides. The field was applied for 3 h across the chamber and incremented continuously from 20 mV to 1.1 V at 12-Hz frequency. Finally, the AC frequency was lowered to 4 Hz at 2 V for 30 min. This lead to detachment of the vesicles from glass slides. GUVs were carefully collected and used immediately for visualization. Images were obtained with a spinning-disk confocal setup (Ultraview; PerkinElmer) that consisted of an inverted microscope (T*i*-E Eclipse; Nikon) with a 14-bit electron-multiplying charge-coupled device camera (C9100; Hamamatsu) using Volocity 6.3 software (PerkinElmer).

Cloning of α-proteobacterial Mic60 homologues into *E. coli* expression vectors

Protein sequences of Mic60 homologues from *R. sphaeroides* ($Mic60^{R.s.}$) and *P. denitrificans* ($Mic60^{P.d.}$) were retrieved from NCBI GenBank (*R. sphaeroides*: KD131, WP_015921743.1; and *P. denitrificans*: PD1222, WP_041529918.1). Coding sequences were synthesized from PCR fragments (GeneArt). Primers containing corresponding restriction sites were used to amplify coding sequences, which were further cloned into expression vector pPROEX HTc for recombinant protein purification.

Protein targeting to the *E. coli* plasma membrane

Coding sequences of Mic60, $Mic60^{IMS}$, and control proteins (Tom20, Tim23, and Tim50) were cloned into pMALp2x vector (a gift from B. Schwappach, New England Biolabs, Inc.) and expressed as periplasm-targeted MBP fusions. BL21(DE3) *E. coli* cells were grown in Terrific Broth media at 37°C in an orbital shaker to OD_{600} 0.6–0.7, and protein expression was induced with 0.5 mM IPTG. Cells were cultured at 18°C for 18 h and harvested by centrifugation at 6,000 *g* for 20 min.

Immunoelectron microscopy of *E. coli* cells and immunogold labeling analysis

BL21(DE3) *E. coli* cells expressing MBP–Mic60 fusion were harvested and chemically fixed in 0.2% glutaraldehyde for 1 h on ice. Washed pellets were resuspended in an equal volume of 10% molten gelatin, spun down, and left to solidify. Gelatin blocks were cut into 1-mm^3 cubes and infiltrated with 2.3 M sucrose overnight. Sample blocks were mounted onto aluminum pins and snap frozen in liquid nitrogen. Ultrathin cryosections were made with a cryoultramicrotome (UC6; Leica Microsystems) with the aid of a cryoimmuno diamond knife (Diatome). Immunolabeling was performed using primary anti-Mic60 antibodies produced in rabbit (1:400; a gift from P. Rehling, University Medical Center Göttingen, Göttingen, Germany). Primary antibodies were detected with protein A gold (10 nm; Cell Microscopy Core, Department of Cell Biology, University Medical Center Utrecht, Netherlands) at 1:50 dilution. Electron micrographs of *E. coli* cells were obtained using a transmission electron microscope (EM900; ZEI SS) equipped with a wide-angle dual-speed 2k charge-coupled device camera using ImageSP software (LI-COR Biosciences).

To analyze where the bulk of the gold particles (bulk of the protein of interest) is located, we evaluated the relative distribution (RD) of the labels. The RD expresses the percentage of specific gold parti-

Downloaded from on March 7, 2017

Published March 2, 2017

cles located to different cellular compartments in the membrane and cytosol. To calculate the RD, we counted gold particles in 27 bacterial cells (n = 27) using ImageJ software (National Institutes of Health). The number of specific gold particles was calculated after extraction from the background (number of gold particles from 27 bacterial cells treated with protein A gold omitting primary staining). To analyze the dispersion of results, the SD was estimated.

Statistical analysis

Error bars represent SD or SEM as indicated in the figure legends.

E. coli subcellular fractionation

BL21(DE3) cells expressing MBP fusion proteins were harvested as described in the Protein targeting to the *E. coli* plasma membrane section. Bacterial pellets were resuspended in 0.7 M sucrose, 150 mM NaCl, 20 mM Hepes, 5 mM $MgSO_4$, 10 mM EDTA, and 1 mg/ml deoxyribonucleaseI, pH 7.4, and spun down at 5,000 *g* for 10 min at 4°C. Washed pellets were resuspended in 10 ml of the same buffer supplemented with 1 mg/ml lysozyme and EDTA-free protease inhibitor cocktail. The suspension was incubated for 30 min at room temperature while gently agitating. After that, 40 ml of distilled water was added to the swirling mixture and placed on ice. Spheroplasts were harvested by centrifugation for 45 min at 20,000 *g* and 4°C. The supernatant contained the periplasmic fraction, and the pellet contained cytoplasmic cylinders. For crude membrane isolation, the pellet was resuspended in 200 mM NaCl, 50 mM Hepes, 5 mM EDTA, and 0.5 mM DTT, pH 7.4, supplemented with protease inhibitors and ruptured by EmulsiFlex (three passes; Avestin). Large cellular debris was pelleted for 15 min at 3,000 rpm and 4°C. Supernatant was ultracentrifuged at 53,000 rpm and 4°C for 3 h (Type 70 Ti rotor; Beckman Coulter). The supernatant contained the cytosolic fraction and the pellet/crude membranes. The membrane-containing pellet was carefully resuspended in the same buffer and ultracentrifuged at 53,000 rpm and 4°C for 40 min (Type 70 Ti rotor). The final pellet was resuspended in 150 mM NaCl, 20 mM Hepes, 5 mM EDTA, and 0.5 mM DTT, pH 7.4, and was additionally homogenized using tissue homogenizer (Schuett Homgen^{plus}). The membrane-containing sample was supplemented with 1% decyl β-D-maltopyranoside and centrifuged at 150,000 *g* and 4°C for 30 min. The supernatant contained an enriched cytoplasmic membrane fraction. Approximately 10 µg of total protein from periplasm, cytoplasm, and cytoplasmic membrane fractions was separated on 12.5% SDS-PAGE. MBP fusions were detected by Western blot analysis using monoclonal antibodies against MBP (Sigma-Aldrich). The quality of subcellular fractionation was monitored by Western blot analysis using primary antibodies raised in mouse against marker proteins of each cellular compartment: β-lactamase for periplasm, GroEL for cytosol, and ATBb for cytoplasmic membrane (all purchased from Abcam).

Yeast strains and growth

Open reading frames of Mic60$^{S.c.}$ with a C-terminal FLAG tag (Mic60$^{S.c.}$-FLAG), of Mic60$^{P.d.}$-FLAG with an N-terminal mitochondrial targeting signal from Mic60$^{S.c.}$, and of Mic60$^{R.s.}$-FLAG with an N-terminal mitochondrial targeting signal from Mic60$^{S.c.}$ were cloned into p413 MET25 vector under the control of the *MET25* promotor. *Δmic60* (Mat a, his3-Δ1 leu2Δ0 met15Δ0 ura3Δ0; fcj1::kanMX4; Alkhaja et al., 2012) were either transformed with the empty plasmid or with plasmids containing the respective construct using the lithium acetate method. The cells were cultured in selective media (0.67% yeast nitrogen base without amino acids, 0.07% His dropout complete supplement mixture lacking histidine [MP Biomedicals], and 2% glucose or 3% glycerol, pH 5.0) and grown at 30°C. For the growth test, the cells were spotted in serial dilutions on selective glycerol plates and were incubated at 18°C. Mitochondria from such cells were isolated by using Zymolyase treatment, Dounce homogenization, and subsequent differential centrifugation. Mic60$^{S.c.}$, Mic60$^{R.s.}$, and Mic60$^{P.d.}$ expression and mitochondrial targeting were monitored by SDS-PAGE and subsequent Western blot analysis of isolated mitochondria using mouse monoclonal antibody against FLAG-tag (Sigma-Aldrich).

EM of yeast cells

For EM, the yeast cells were precultured at 30°C in selective liquid medium containing 2% glucose (1.7 g/liter yeast nitrogen base, 2 g/liter His dropout mix, 5 g/liter ammonium sulfate, and 20 g/liter glucose). The cells were then transferred into selective liquid medium containing 3% glycerol (1.7 g/liter yeast nitrogen base, 2 g/liter His dropout mix, 5 g/liter ammonium sulfate, and 30 g/liter glycerol) and harvested in the logarithmic growth phase. The yeast cells were fixed for 30 min in 2% glutaraldehyde. After several washing steps, the cells were incubated with Zymolyase solution (0.1 mg/ml Zymolyase 100T and 0.5% 2-mercaptoethanol in 1× PBS/10% sorbitol [wt/vol]) for 15 min at room temperature to remove the cell wall. After a second fixation with 1% osmium tetroxide (30 min), the cells were poststained with 1% uranyl acetate for 2 h. After dehydration in a graded ethanol series and propylene oxide, the cells were embedded in epoxide resin (Agar 100; Plano). Ultrathin sections were examined using a transmission electron microscope (CM 120; Philips), and images were taken with a CMOS camera (TemCam F416; TVIPS).

Light microscopy

For light microscopy, the yeast cells were transformed with pVT100U-mitoGFP and were grown in selective medium containing 2% glucose (1.7 g/liter yeast nitrogen base, 2 g/liter His-ura dropout mix, 5 g/liter ammonium sulfate, and 20 g/liter glucose). Confocal images were recorded with an SP8 confocal microscope (Leica Microsystems). Z image series were taken, and maximum projections of stacks are displayed.

Online supplemental material

Fig. S1 displays controls for the in vitro reconstitution and membrane deformation assays. Fig. S2 is the accompanying figure for the bacterial plasma membrane deformation experiments. Fig. S3 shows the primary sequence alignment of yeast and α-proteobacterial Mic60s as well as the mitochondrial targeting of Mic60$^{P.d.}$ and Mic60$^{R.s.}$ and growth test experiments for the various yeast strains.

Acknowledgments

We thank P. Rehling for continuous discussion, advice, and materials and N. Denkert for critical discussions. We thank S. Callegari for helpful comments on the manuscript and M. Hoppert and T. Ruhwedel for practical help with the EM. We thank A.B. Schendzielorz for advice and help with yeast experiments and P. Halder for assistance with circular dichroism spectroscopy measurements.

This work was supported by the Deutsche Forschungsgemeinschaft: SFB 803 project B09 (to M. Barbot), SFB 1190 projects 1 and 12 (to D. Tarasenko, D.C. Jans, and S. Jakobs), and FOR 1905 TP1 (to M. Meinecke).

The authors declare no competing financial interests.

Author contributions: M. Meinecke, D. Tarasenko, and M. Barbot conceived and designed the study. All authors performed experiments and analyzed the data: D. Tarasenko performed in vitro reconstitution,

Downloaded from on March 7, 2017

Published March 2, 2017

membrane deformation, and, together with W. Möbius and B. Sadowski, bacterial experiments. M. Barbot performed orientation and mitochondrial targeting experiments. B. Kroppen performed GUV experiments. D.C. Jans, G. Heim, and S. Jakobs performed fluorescence microscopy and EM of yeast mitochondria. M. Meinecke wrote the manuscript with the input of D. Tarasenko, M. Barbot, and S. Jakobs.

Submitted: 9 September 2016
Revised: 4 January 2017
Accepted: 13 January 2017

References

Aaltonen, M.J., J.R. Friedman, C. Osman, B. Salin, J.P. di Rago, J. Nunnari, T. Langer, and T. Tatsuta. 2016. MICOS and phospholipid transfer by Ups2-Mdm35 organize membrane lipid synthesis in mitochondria. *J. Cell Biol.* 213:525–534. http://dx.doi.org/10.1083/jcb.201602007

Alkhaja, A.K., D.C. Jans, M. Nikolov, M. Vukotic, O. Lytovchenko, F. Ludewig, W. Schliebs, D. Riedel, H. Urlaub, S. Jakobs, and M. Deckers. 2012. MIN OS1 is a conserved component of mitofilin complexes and required for mitochondrial function and cristae organization. *Mol. Biol. Cell.* 23:247–257. http://dx.doi.org/10.1091/mbc.E11-09-0774

Barbot, M., and M. Meinecke. 2016. Reconstitutions of mitochondrial inner membrane remodeling. *J. Struct. Biol.* 196:20–28. http://dx.doi.org/10.1016/j.jsb.2016.07.014

Barbot, M., D.C. Jans, C. Schulz, N. Denkert, B. Kroppen, M. Hoppert, S. Jakobs, and M. Meinecke. 2015. Mic10 oligomerizes to bend mitochondrial inner membranes at cristae junctions. *Cell Metab.* 21:756–763. http://dx.doi.org/10.1016/j.cmet.2015.04.006

Bock, E., and G. Heinrich. 1971. Struktur- und Funktionsänderungen in reaktivierenden Zellen von *Nitrobacter winogradskyi* Buch [Structural and functional changes in reactivating cells of *Nitrobacter winogradskyi* Buch]. *Arch. Mikrobiol.* 77:349–365. http://dx.doi.org/10.1007/BF00425038

Bohnert, M., L.S. Wenz, R.M. Zerbes, S.E. Horvath, D.A. Stroud, K. von der Malsburg, J.M. Müller, S. Oeljeklaus, I. Perschil, B. Warscheid, et al. 2012. Role of mitochondrial inner membrane organizing system in protein biogenesis of the mitochondrial outer membrane. *Mol. Biol. Cell.* 23:3948–3956. http://dx.doi.org/10.1091/mbc.E12-04-0295

Bohnert, M., R.M. Zerbes, K.M. Davies, A.W. Mühleip, H. Rampelt, S.E. Horvath, T. Boenke, A. Kram, I. Perschil, M. Veenhuis, et al. 2015. Central role of Mic10 in the mitochondrial contact site and cristae organizing system. *Cell Metab.* 21:747–755. http://dx.doi.org/10.1016/j.cmet.2015.04.007

D'Amici, G.M., S. Rinalducci, L. Murgiano, F. Italiano, and L. Zolla. 2010. Oligomeric characterization of the photosynthetic apparatus of *Rhodobacter sphaeroides* R26.1 by nondenaturing electrophoresis methods. *J. Proteome Res.* 9:192–203. http://dx.doi.org/10.1021/pr9005052

Friedman, J.R., A. Mourier, J. Yamada, J.M. McCaffery, and J. Nunnari. 2015. MICOS coordinates with respiratory complexes and lipids to establish mitochondrial inner membrane architecture. *eLife.* 4:e07739. http://dx.doi.org/10.7554/eLife.07739

Gleisner, M., B. Kroppen, C. Fricke, N. Teske, T.T. Kliesch, A. Janshoff, M. Meinecke, and C. Steinem. 2016. Epsin N-terminal homology domain (ENTH) activity as a function of membrane tension. *J. Biol. Chem.* 291:19953–19961. http://dx.doi.org/10.1074/jbc.M116.731612

Guarani, V., E.M. McNeill, J.A. Paulo, E.L. Huttlin, F. Fröhlich, S.P. Gygi, D. Van Vactor, and J.W. Harper. 2015. QIL1 is a novel mitochondrial protein required for MICOS complex stability and cristae morphology. *eLife.* 4:e06256. http://dx.doi.org/10.7554/eLife.06265

Harner, M., C. Körner, D. Walther, D. Mokranjac, J. Kaesmacher, U. Welsch, J. Griffith, M. Mann, F. Reggiori, and W. Neupert. 2011. The mitochondrial contact site complex, a determinant of mitochondrial architecture. *EMBO J.* 30:4356–4370. http://dx.doi.org/10.1038/emboj.2011.379

Hoppins, S., S.R. Collins, A. Cassidy-Stone, E. Hummel, R.M. Devay, L.L. Lackner, B. Westermann, M. Schuldiner, J.S. Weissman, and J. Nunnari. 2011. A mitochondrial-focused genetic interaction map reveals a scaffold-like complex required for inner membrane organization in mitochondria. *J. Cell Biol.* 195:323–340. http://dx.doi.org/10.1083/jcb.201107053

Hu, J., H. Qin, F.P. Gao, and T.A. Cross. 2011. A systematic assessment of mature MBP in membrane protein production: overexpression, membrane targeting and purification. *Protein Expr. Purif.* 80:34–40. http://dx.doi.org/10.1016/j.pep.2011.06.001

Huynen, M.A., M. Mühlmeister, K. Gotthardt, S. Guerrero-Castillo, and U. Brandt. 2016. Evolution and structural organization of the mitochondrial contact site (MICOS) complex and the mitochondrial intermembrane space bridging (MIB) complex. *Biochim. Biophys. Acta.* 1863:91–101. http://dx.doi.org/10.1016/j.bbamcr.2015.10.009

Jans, D.C., C.A. Wurm, D. Riedel, D. Wenzel, F. Stagge, M. Deckers, P. Rehling, and S. Jakobs. 2013. STED super-resolution microscopy reveals an array of MINOS clusters along human mitochondria. *Proc. Natl. Acad. Sci. USA.* 110:8936–8941. http://dx.doi.org/10.1073/pnas.1301820110

John, G.B., Y. Shang, L. Li, C. Renken, C.A. Mannella, J.M. Selker, L. Rangell, M.J. Bennett, and J. Zha. 2005. The mitochondrial inner membrane protein mitofilin controls cristae morphology. *Mol. Biol. Cell.* 16:1543–1554. http://dx.doi.org/10.1091/mbc.E04-08-0697

Komeili, A., H. Vali, T.J. Beveridge, and D.K. Newman. 2004. Magnetosome vesicles are present before magnetite formation, and MamA is required for their activation. *Proc. Natl. Acad. Sci. USA.* 101:3839–3844. http://dx.doi.org/10.1073/pnas.0400391101

Körner, C., M. Barrera, J. Dukanovic, K. Eydt, M. Harner, R. Rabl, F. Vogel, D. Rapaport, W. Neupert, and A.S. Reichert. 2012. The C-terminal domain of Fcj1 is required for formation of crista junctions and interacts with the TOB/SAM complex in mitochondria. *Mol. Biol. Cell.* 23:2143–2155. http://dx.doi.org/10.1091/mbc.E11-10-0831

Krüger, V., M. Deckers, M. Hildenbeutel, M. van der Laan, M. Hellmers, C. Dreker, M. Preuss, J.M. Herrmann, P. Rehling, R. Wagner, and M. Meinecke. 2012. The mitochondrial oxidase assembly protein1 (Oxa1) insertase forms a membrane pore in lipid bilayers. *J. Biol. Chem.* 287:33314–33326. http://dx.doi.org/10.1074/jbc.M112.387563

Mannella, C.A. 2006. Structure and dynamics of the mitochondrial inner membrane cristae. *Biochim. Biophys. Acta.* 1763:542–548. http://dx.doi.org/10.1016/j.bbamcr.2006.04.006

McMahon, H.T., and E. Boucrot. 2011. Molecular mechanism and physiological functions of clathrin-mediated endocytosis. *Nat. Rev. Mol. Cell Biol.* 12:517–533. http://dx.doi.org/10.1038/nrm3151

Montilla-Martinez, M., S. Beck, J. Klümper, M. Meinecke, W. Schliebs, R. Wagner, and R. Erdmann. 2015. Distinct pores for peroxisomal import of PTS1 and PTS2 proteins. *Cell Reports.* 13:2126–2134. http://dx.doi.org/10.1016/j.celrep.2015.11.016

Muñoz-Gómez, S.A., C.H. Slamovits, J.B. Dacks, K.A. Baier, K.D. Spencer, and J.G. Wideman. 2015. Ancient homology of the mitochondrial contact site and cristae organizing system points to an endosymbiotic origin of mitochondrial cristae. *Curr. Biol.* 25:1489–1495. http://dx.doi.org/10.1016/j.cub.2015.04.006

Nudelman, H., and R. Zarivach. 2014. Structure prediction of magnetosome-associated proteins. *Front. Microbiol.* 5:9. http://dx.doi.org/10.3389/fmicb.2014.00009

Ott, C., K. Ross, S. Straub, B. Thiede, M. Götz, C. Goosmann, M. Krischke, M.J. Mueller, G. Krohne, T. Rudel, and V. Kozjak-Pavlovic. 2012. Sam50 functions in mitochondrial intermembrane space bridging and biogenesis of respiratory complexes. *Mol. Cell. Biol.* 32:1173–1188. http://dx.doi.org/10.1128/MCB.06388-11

Pellegrini, L., and L. Scorrano. 2007. A cut short to death: Parl and Opa1 in the regulation of mitochondrial morphology and apoptosis. *Cell Death Differ.* 14:1275–1284. http://dx.doi.org/10.1038/sj.cdd.4402145

Privé, G.G. 2007. Detergents for the stabilization and crystallization of membrane proteins. *Methods.* 41:388–397. http://dx.doi.org/10.1016/j.ymeth.2007.01.007

Rabl, R., V. Soubannier, R. Scholz, F. Vogel, N. Mendl, A. Vasiljev-Neumeyer, C. Körner, R. Jagasia, T. Keil, W. Baumeister, et al. 2009. Formation of cristae and crista junctions in mitochondria depends on antagonism between Fcj1 and Su *e/g*. *J. Cell Biol.* 185:1047–1063. http://dx.doi.org/10.1083/jcb.200811099

Scorrano, L., M. Ashiya, K. Buttle, S. Weiler, S.A. Oakes, C.A. Mannella, and S.J. Korsmeyer. 2002. A distinct pathway remodels mitochondrial cristae and mobilizes cytochrome *c* during apoptosis. *Dev. Cell.* 2:55–67. http://dx.doi.org/10.1016/S1534-5807(01)00116-2

Shemesh, T., R.W. Klemm, F.B. Romano, S. Wang, J. Vaughan, X. Zhuang, H. Tukachinsky, M.M. Kozlov, and T.A. Rapoport. 2014. A model for the generation and interconversion of ER morphologies. *Proc. Natl. Acad. Sci. USA.* 111:E5243–E5251. http://dx.doi.org/10.1073/pnas.1419997111

Simunovic, M., and P. Bassereau. 2014. Reshaping biological membranes in endocytosis: crossing the configurational space of membrane-protein interactions. *Biol. Chem.* 395:275–283. http://dx.doi.org/10.1515/hsz-2013-0242

Strauss, M., G. Hofhaus, R.R. Schröder, and W. Kühlbrandt. 2008. Dimer ribbons of ATP synthase shape the inner mitochondrial membrane. *EMBO J.* 27:1154–1160. http://dx.doi.org/10.1038/emboj.2008.35

Downloaded from on March 7, 2017

Published March 2, 2017

Tucker, J.D., C.A. Siebert, M. Escalante, P.G. Adams, J.D. Olsen, C. Otto, D.L. Stokes, and C.N. Hunter. 2010. Membrane invagination in *Rhodobacter sphaeroides* is initiated at curved regions of the cytoplasmic membrane, then forms both budded and fully detached spherical vesicles. *Mol. Microbiol.* 76:833–847. http://dx.doi.org/10.1111/j.1365-2958.2010.07153.x

van der Laan, M., M. Meinecke, J. Dudek, D.P. Hutu, M. Lind, I. Perschil, B. Guiard, R. Wagner, N. Pfanner, and P. Rehling. 2007. Motor-free mitochondrial presequence translocase drives membrane integration of preproteins. *Nat. Cell Biol.* 9:1152–1159.

Vogel, F., C. Bornhövd, W. Neupert, and A.S. Reichert. 2006. Dynamic subcompartmentalization of the mitochondrial inner membrane. *J. Cell Biol.* 175:237–247. http://dx.doi.org/10.1083/jcb.200605138

von der Malsburg, K., J.M. Müller, M. Bohnert, S. Oeljeklaus, P. Kwiatkowska, T. Becker, A. Loniewska-Lwowska, S. Wiese, S. Rao, D. Milenkovic, et al. 2011. Dual role of mitofilin in mitochondrial membrane organization and protein biogenesis. *Dev. Cell.* 21:694–707. http://dx.doi.org/10.1016/j.devcel.2011.08.026

Walser, P.J., N. Ariotti, M. Howes, C. Ferguson, R. Webb, D. Schwudke, N. Leneva, K.J. Cho, L. Cooper, J. Rae, et al. 2012. Constitutive formation of caveolae in a bacterium. *Cell.* 150:752–763. http://dx.doi.org/10.1016/j.cell.2012.06.042

Wurm, C.A., and S. Jakobs. 2006. Differential protein distributions define two sub-compartments of the mitochondrial inner membrane in yeast. *FEBS Lett.* 580:5628–5634. http://dx.doi.org/10.1016/j.febslet.2006.09.012

Xie, J., M.F. Marusich, P. Souda, J. Whitelegge, and R.A. Capaldi. 2007. The mitochondrial inner membrane protein mitofilin exists as a complex with SAM50, metaxins 1 and 2, coiled-coil-helix coiled-coil-helix domain-containing protein 3 and 6 and DnaJC11. *FEBS Lett.* 581:3545–3549. http://dx.doi.org/10.1016/j.febslet.2007.06.052

Zerbes, R.M., M. Bohnert, D.A. Stroud, K. von der Malsburg, A. Kram, S. Oeljeklaus, B. Warscheid, T. Becker, N. Wiedemann, M. Veenhuis, et al. 2012. Role of MINOS in mitochondrial membrane architecture: cristae morphology and outer membrane interactions differentially depend on mitofilin domains. *J. Mol. Biol.* 422:183–191. http://dx.doi.org/10.1016/j.jmb.2012.05.004

Zerbes, R.M., P. Höß, N. Pfanner, M. van der Laan, and M. Bohnert. 2016. Distinct roles of Mic12 and Mic27 in the mitochondrial contact site and cristae organizing system. *J. Mol. Biol.* 428:1485–1492. http://dx.doi.org/10.1016/j.jmb.2016.02.031

Zimmerberg, J., and M.M. Kozlov. 2006. How proteins produce cellular membrane curvature. *Nat. Rev. Mol. Cell Biol.* 7:9–19. http://dx.doi.org/10.1038/nrm1784

Downloaded from on March 7, 2017